


# Sensitivity Enhancement and Random Telegraph Noise in Magnetic Tunnel Junctions with Compensated Anisotropy

Guanyang He<sup>✉,\*</sup>, Yiou Zhang<sup>✉</sup>, and Gang Xiao<sup>✉,†</sup>

*Department of Physics, Brown University, Providence, Rhode Island 02912, USA*

 (Received 21 September 2021; revised 11 January 2023; accepted 23 January 2023; published 27 February 2023)

We demonstrate the manipulation of perpendicular magnetic anisotropy (PMA) in magnetic tunnel junctions (MTJs) by varying the layer stacks and temperature. PMA is tuned to compensate the shape anisotropy, giving a nonhysteretic magnetic response, a noteworthy sensitivity enhancement, and a field detectability of  $1.8 \text{ nT}/\sqrt{\text{Hz}}$  at 100 kHz. Such a method is further exemplified in multiple MTJs, providing a solution to obtain desired sensitivities and operating temperatures. Additionally, the electronic noise of this MTJ is revealed as a random telegraph noise (RTN) due to a generation-recombination process. The observed voltage-dependent RTN could potentially be applied to true random number generators.

DOI: [10.1103/PhysRevApplied.19.024069](https://doi.org/10.1103/PhysRevApplied.19.024069)

## I. INTRODUCTION

A magnetic tunnel junction (MTJ) is a magnetoresistance device extensively applied in magnetic field sensing or biomedical imaging, with its advantages including large signals, low power consumption, and CMOS compatibility [1,2]. For magnetic sensors based on MTJs, the elimination of hysteresis has always been critical, where solutions related to the hard-axis bias field, shape anisotropy, superparamagnetism, and interfacial perpendicular magnetic anisotropy (PMA) have all been explored [3–6]. While most linearization strategies come at the cost of sensitivity, specific hard-axis bias fields can actually enhance the sensitivity [7,8]. Since PMA with its easy tunability [9,10] can also act as an effective field in the out-of-plane direction, similar enhancement may be expected. Focusing on this idea, we have already shown that the compensation of magnetic anisotropy leads to excellent sensing performances in sensors based on the anomalous Hall effect (AHE) [11,12]. In this work, we demonstrate that the introduction of PMA in MTJ sensors not only eliminates the hysteresis but also boosts the sensitivity. By optimizing the PMA strength using varying layer thicknesses and annealing treatments, we characterize the magnetic sensing performances of this class of MTJs in a broad temperature range from 140 to 400 K.

## II. EXPERIMENT

Following relevant literature [13–15], we use a modified layer structure in our MTJs, which effectively induces

PMA in the synthetic free layer (FL); it is sequenced as: Si/SiO<sub>2</sub>/Ta(50)/Ru(150)/Ta(100)/MgO(16)/FL/MgO(27)/Co<sub>40</sub>Fe<sub>40</sub>B<sub>20</sub>(30)/Ru(8.5)/Co<sub>50</sub>Fe<sub>50</sub>(30)/Ir<sub>22</sub>Mn<sub>78</sub>(180)/Ru(100)/Ta(100). The numbers in parentheses represent the thickness of each layer in angstroms. The FL consists of Co<sub>40</sub>Fe<sub>40</sub>B<sub>20</sub>(9)/W(*t<sub>W</sub>*)/Co<sub>40</sub>Fe<sub>40</sub>B<sub>20</sub>(*t<sub>CFB</sub>*) where the two Co-Fe-B layers are coupled by Ruderman–Kittel–Kasuya–Yosida (RKKY) interaction through the W spacer. We use magnetron sputtering to deposit the complete MTJ with a base pressure of  $2 \times 10^{-8}$  torr. Photolithography and physical ion milling are used to define MTJ elements into an oval shape of a lateral size of  $7 \times 10.5 \mu\text{m}^2$ . After fabrication, thermal annealing is performed at temperature  $T_a$  for one hour in high vacuum, under a magnetic field of 0.45 T along the long-axis direction of the MTJ oval. In all our magneto-transport measurements conducted with a Quantum Design® Physical Property Measurement System, eight identical MTJs are connected in series as a sensor unit, exposed to in-plane magnetic fields applied in the long-axis direction (magnetic easy axis) of each MTJ oval. The resistance-area product of MTJs is typically  $60 \text{ k}\Omega \mu\text{m}^2$ , giving a total resistance of 8 kΩ for eight MTJ elements in series. Thus, the contact resistance (around 1 Ω) is negligible in our two-probe electrical measurements. The MTJ sensor is powered by batteries and connected in series with a voltage divider resistor during measurements. The bias voltage across the MTJ sensor is 0.3 V, or 37.5 mV per MTJ element. The field sensitivity is experimentally determined by the voltage response to a modulating field ( $\delta H = 0.3 \text{ Oe}$ ) at 5 Hz. In the literature, the sensitivity is roughly related to the magnetic anisotropy through the transfer curve [16,17]. Unless the sensor is hysteresis-free, the sensitivity overestimated this way could deviate from the real values in low-field measurements [18].

\*guanyang\_he@pku.edu.cn

†Gang\_Xiao@brown.edu

### III. RESULTS AND DISCUSSION

Figure 1 shows the tunneling magnetoresistance ratio (TMR) transfer curves of MTJs at 300 K with various layer thicknesses and annealing temperatures ( $T_a$ ). In Fig. 1(a), while fixing the Co-Fe-B thickness  $t_{\text{CFB}} = 14.3 \text{ \AA}$  and  $T_a = 300 \text{ }^\circ\text{C}$ , we vary the W spacer thickness  $t_W$  from 8 to 4  $\text{\AA}$ . The coercivity collapses and the saturation field increases, implying that PMA strength is weaker for thicker spacer. This is because in the composite free layer  $\text{Co}_{40}\text{Fe}_{40}\text{B}_{20}(9)/\text{W}(t_W)/\text{Co}_{40}\text{Fe}_{40}\text{B}_{20}(t_{\text{CFB}})$ , two Co-Fe-B layers are coupled by RKKY interaction. Both sides of the FL are neighbored with MgO for the interfacial PMA [14]. In the first 9- $\text{\AA}$ -thick Co-Fe-B layer, the magnetic moments are mostly in the out-of-plane direction; the moments in the second Co-Fe-B layer tend to be aligned the same way due to their magnetic coupling. Such coupling effectively serves as an additional source of PMA. Therefore, if the increment in spacer thickness  $t_W$  impairs this coupling, the PMA in the second Co-Fe-B layer would become weaker. This is likely because the RKKY strength is reported to have nonmonotonic or oscillatory relations with the spacer layer thickness [19–21]. A similar trend is observed when  $t_{\text{CFB}}$  is varied with  $t_W = 6 \text{ \AA}$ ,  $T_a = 300 \text{ }^\circ\text{C}$  fixed, as shown in Fig. 1(b). This is a

straightforward result of PMA decreasing with film thickness. Finally, as shown in Fig. 1(c), PMA strength is also enhanced as  $T_a$  increases from 280 to 300  $^\circ\text{C}$ , for  $t_W = 6 \text{ \AA}$  and  $t_{\text{CFB}} = 13.5 \text{ \AA}$ . Combining these results, stronger PMA is present in MTJs with thinner Co-F-eB layer and W spacer, as well as higher  $T_a$ . The PMA in the free layer of MTJs reduces and eventually eliminates the magnetic hysteresis, which also leads to large saturation fields and low TMR ratios.

Figure 2(a) shows the TMR transfer curves from 140 to 400 K in MTJs with  $t_W = 6 \text{ \AA}$ , where  $t_{\text{CFB}} = 13.9 \text{ \AA}$  and  $T_a = 300 \text{ }^\circ\text{C}$  are fixed. While the saturation field increases monotonically as temperature decreases, the coercivity increases after reaching a minimum at 340 K, as shown in Fig. 2(b). As a crucial factor influencing the transfer curves, the PMA strength in MTJs is known to be tunable by temperature [22]. However, the uncommon temperature dependence of the transfer curves here cannot be explained solely by a temperature-dependent PMA, which should be derived from regions with different PMA strengths in the MTJ free layer. This inhomogeneity of PMA could originate from a thickness variation or boundary effect. To simplify the scenario, we assume the existence of “*P*-regions” with strong PMA, and “*I*-regions” with weak

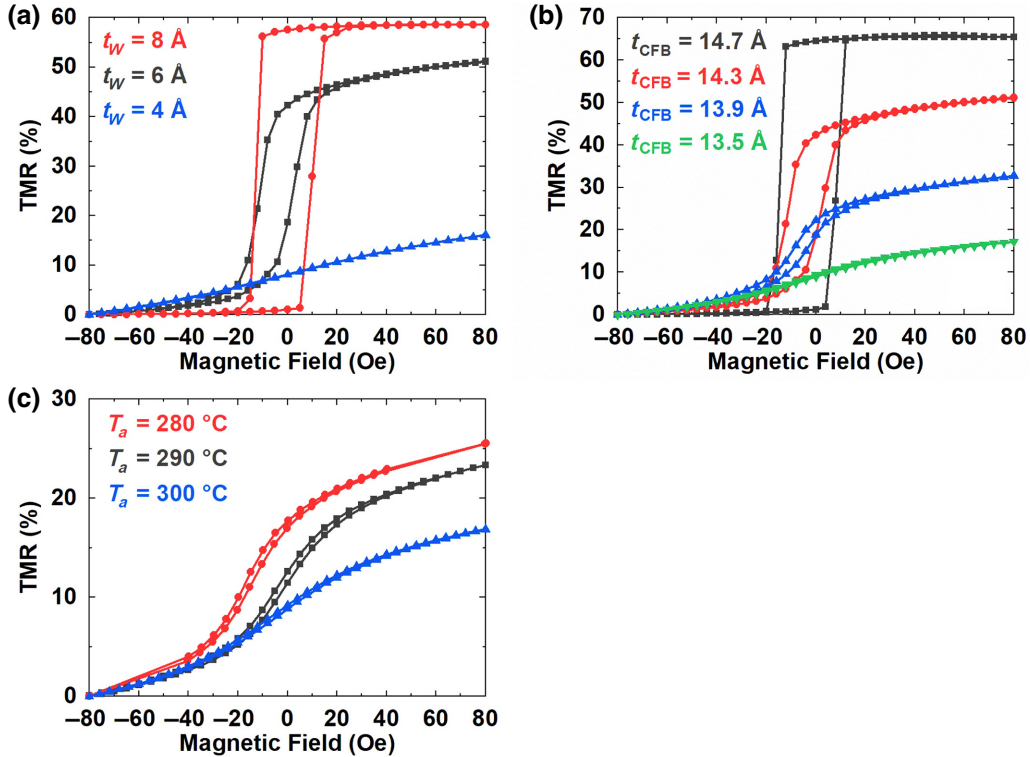


FIG. 1. TMR ratio versus magnetic field (transfer curve) of MTJs incorporating a coupled free layer of  $\text{Co}_{40}\text{Fe}_{40}\text{B}_{20}(9 \text{ \AA})/\text{W}(t_W)/\text{Co}_{40}\text{Fe}_{40}\text{B}_{20}(t_{\text{CFB}})$ , with (a) different W spacer layer thickness  $t_W$ , (b) different Co-Fe-B layer thickness  $t_{\text{CFB}}$ , and (c) different annealing temperature  $T_a$ . The magnetic fields are applied in the in-plane long-axis direction of the MTJ oval, and the measurement temperature is 300 K.

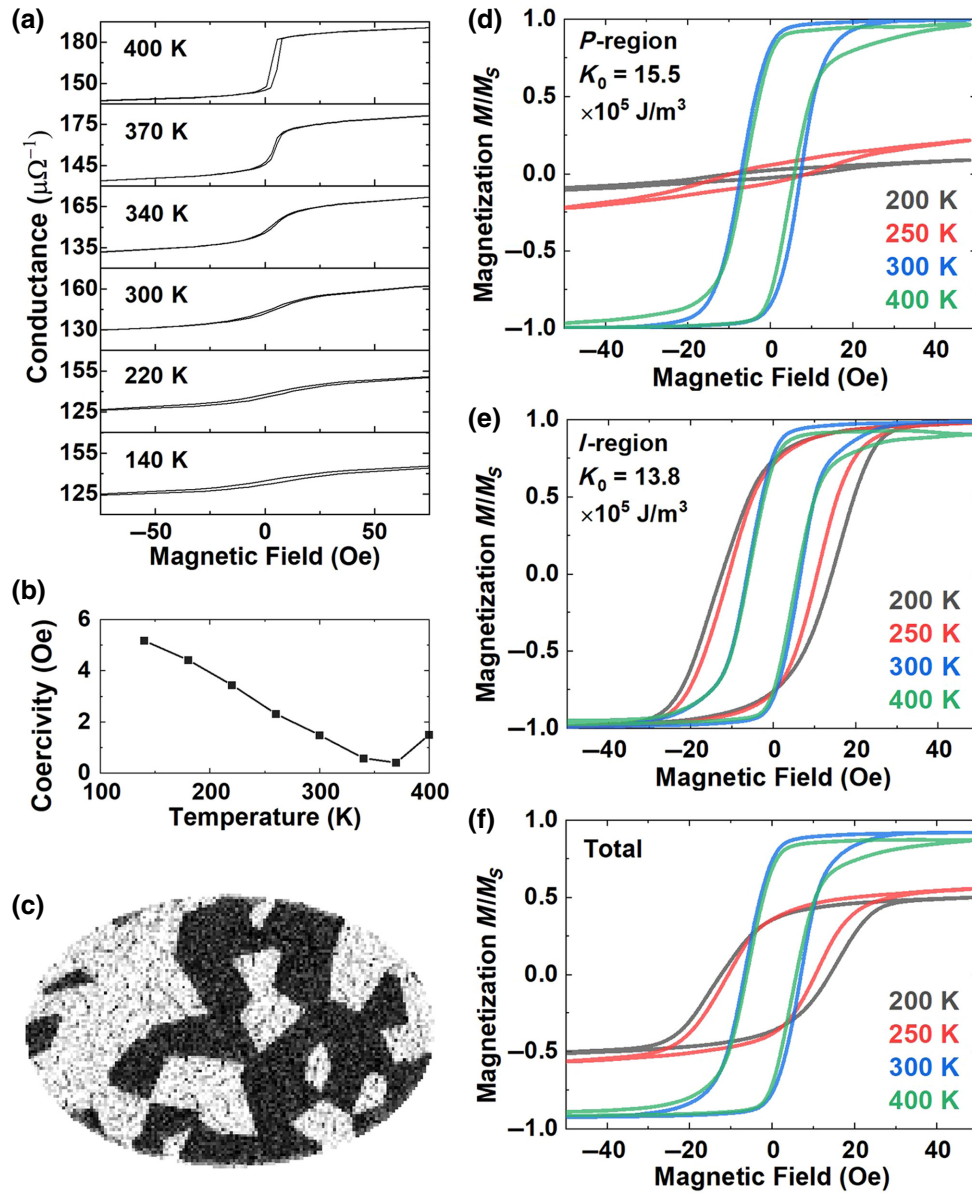


FIG. 2. (a) Magneto-transport measurement of one MTJ ( $t_W = 6 \text{ \AA}$ ,  $t_{\text{CFB}} = 13.9 \text{ \AA}$ ,  $T_a = 300 \text{ }^\circ\text{C}$ ), from 140 to 400 K. (b) Temperature dependence of magnetic coercivity  $H_c$  obtained from (a). (c) Schematic diagram of the micromagnetic simulation of the MTJ free layer, with randomly distributed *P*-regions and *I*-regions. Brighter colors indicate stronger magnetizations in the out-of-plane direction, and this magnetization is obtained at 250 K, 50 Oe in-plane field. (d) Magnetization transfer curves of the *P*-region from simulation. (e) Magnetization transfer curves of the *I*-region from simulation. (f) Total magnetization transfer curves of the MTJ free layer from simulation. Magnetic field is applied along the in-plane long-axis direction of the MTJ oval.

PMA (more in-plane magnetization). Nevertheless, a direct observation of these two regions with a magneto-optic Kerr effect (MOKE) microscope or magnetic force microscope (MFM) is difficult, because a thick protective capping layer is used to preserve the interface of Co-Fe-B/W or Co-Fe-B/MgO from where PMA originates. Such capping layer suppresses optical signals from Co-Fe-B for MOKE and elongates the lift-off distance for the MFM tip. Therefore, using thinner capping layers in this MTJ device would be appealing in future

studies, or measuring it using x-ray photoemission electron microscopy.

To manifest the behavior of a MTJ free layer with *P*-regions and *I*-regions, micromagnetic simulations are performed by Mumax software. At each temperature and external field, the simulation runs for 5 ns to account for the dynamic effect at finite temperature. In the simulation the exchange stiffness of the Co-Fe-B free layer is appropriately set as  $15 \text{ pJ/m}$ , and the saturation magnetization is temperature ( $T$ ) dependent as  $M_0[1 - (T/T_C)^{1.5}]$  [23], with

$M_0 = 1.46 \times 10^6$  A/m,  $T_C = 1120$  K [24]. The Landau-Lifshitz damping coefficient is 0.1. The shape of free layer is set to be an oval with a major axis of  $10.5 \mu\text{m}$ , a minor axis of  $7 \mu\text{m}$ , and a thickness of  $13.9 \text{ \AA}$ ; every setting stays the same as for the sample of Fig. 2(a). The temperature-dependent PMA takes the form of  $K_0[1 - (T/T_C)^{1.5}]^3$  [23]; for the  $P$ -region,  $K_0 = 15.5 \times 10^5 \text{ J/m}^3$  matches well with experiments, and for the  $I$ -region  $K_0 = 13.8 \times 10^5 \text{ J/m}^3$ . Regions of different PMA are considered to be weakly exchange-coupled across grain boundaries as in the literature [25], with 50% exchange coupling strength. Two kinds of regions are randomly distributed in the MTJ oval, with a configuration shown in Fig. 2(c);  $P$ -regions with stronger PMA are exhibited with brighter colors. The magnetization transfer curves of the  $P$ -region, the  $I$ -region, and the total free layer are shown in Figs. 2(d)–2(f), respectively. At high temperatures above 300 K, PMA is so negligible that the two regions show similar transfer curves. As temperature drops to around 200 K, the saturation field in Fig. 2(f) increases due to the enhanced PMA in  $P$ -regions. The magnetic moments in  $P$ -regions can hardly be aligned with the in-plane magnetic fields because of the strong PMA, and in Fig. 2(d) the saturation field rises beyond the field range of simulation. The increased saturation field is also accompanied by smaller permeabilities in both Figs. 2(d) and 2(f). Meanwhile, the coercivity is increased with

decreasing temperature in Fig. 2(f), which is mostly contributed by the hysteretic  $I$ -regions as in Fig. 2(e). With dominant in-plane shape anisotropies and multidomain features, clear coercivity exists in  $I$ -regions and increases at lower temperatures due to the thermal-assisted domain nucleation and propagation [26]. Therefore, the characteristics of simulation in Fig. 2(f) are understood and correspond well qualitatively with the experimental results in Fig. 2(a). What is missing is the minimum of coercivity in Fig. 2(a) with no correspondence in Fig. 2(f). Such vanishing coercivity only appears at the spin reorientation from out-of-plane to in-plane direction in the free layer, where PMA is just enough to compensate the in-plane anisotropy. Such a critical compensation is difficult to find in simulations, but we illustrate it more with experimental results in the next paragraph. In addition, simulations for another configuration of  $P$ -regions and  $I$ -regions are shown in Fig. 3, where the two regions are more well defined instead of randomly distributed. The increase of coercivity due to domain nucleation and propagation at low temperatures is not matched in Fig. 3, implying that the random distribution of the two regions is closer to that of the experiments.

Generally speaking, magnetic moments in  $I$ -regions are more responsive to external in-plane fields, contributing more sensitivity and noise, and the moments in the

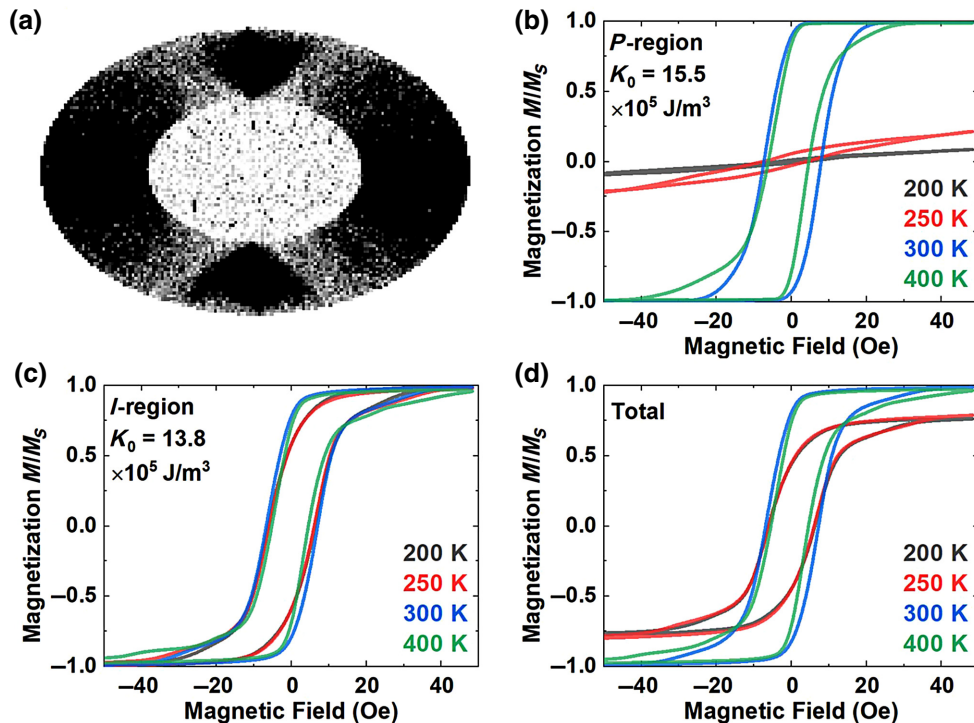


FIG. 3. (a) Schematic diagram of the micromagnetic simulation of the MTJ free layer, with two well-defined  $P$ -region and  $I$ -region. Brighter colors indicate stronger magnetizations in the out-of-plane direction, and this magnetization is obtained at 200 K, 50 Oe in-plane field. (b) Magnetization transfer curves of the  $P$ -region from simulation. (c) Magnetization transfer curves of the  $I$ -region from simulation. (d) Total magnetization transfer curves of the MTJ free layer from simulation.

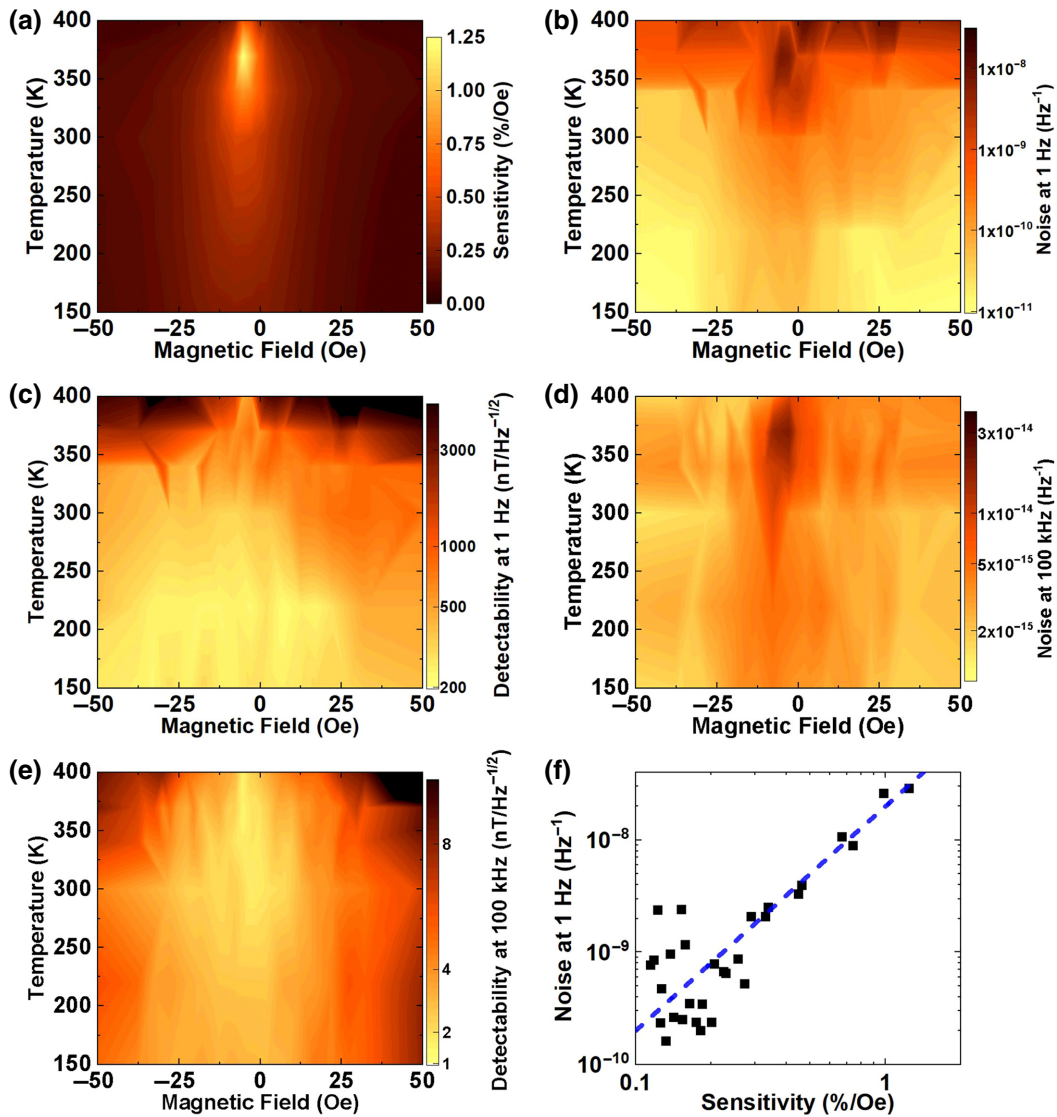


FIG. 4. Magnetic sensing properties of a MTJ with ( $t_W = 6 \text{ \AA}$ ,  $t_{\text{CFB}} = 13.9 \text{ \AA}$ ,  $T_a = 300 \text{ }^\circ\text{C}$ ), measured at different temperatures. (a) Magnetic sensitivity. (b) Normalized noise at 1 Hz. (c) Magnetic field detectability at 1 Hz. (d) Normalized noise at 100 kHz. (e) Magnetic field detectability at 100 kHz. (f) Quadratic scaling relation between noise and sensitivity at 1 Hz, at 370 K measurement temperature.

$P$ -region make the overall performance less coercive. The sensitivity maps of this MTJ under different temperatures and magnetic fields are given in Fig. 4(a). It is noteworthy that the maximum sensitivity is reached at 370 K, where coercivity is the smallest, yet the slope of the dc transfer curve is not the largest in Fig. 2(a). It corresponds to the spin reorientation in the free layer, where magnetic moments can rotate freely and contribute very large sensitivity. This reveals an important fact that the actual sensitivity to small magnetic fields cannot be solely estimated from the transfer curve slope. Even tiny coercivity can lock the magnetic moments in low-field measurements, regardless of the overall transfer curve. The noise spectral density is obtained and normalized by the bias

voltage on the sensor, and its values at 1 Hz and 100 kHz are, respectively, shown in Figs. 4(b) and 4(d). At both frequencies, the noise level is high in the sensing region and low at large fields (magnetically saturated), which implies that it is mostly contributed by magnetic fluctuation [27]. In Figs. 4(c) and 4(e), the sensor detectability at 1 Hz and 100 kHz is calculated by the ratio between the noise and the sensitivity. In Table I, our result is compared with those of MTJs adopting other linearization strategies, and AHE sensors. Our MTJ sensors with compensated magnetic anisotropy exhibit higher sensitivity than most of the others. MTJs with a soft pinned free layer also show high sensitivity, yet their magnetic field detectability is worse than that of our MTJs. Therefore, our sensor

TABLE I. Sensitivity and detectability of our MTJs and MTJ sensors involving other linearization strategies. Two AHE sensors with compensated magnetic anisotropy are also included. For fair comparison of sensitivity, MTJ sensors are assumed to be voltage biased by 100 mV and AHE sensors to be current biased by 1 mA. Also, the magnetic field detectability at 1 Hz  $S_T^{1\text{Hz}}$  is normalized by the active sensing area  $A$ . All results are measured without magnetic flux concentrators, and obtained at room temperature.

Ref.	Linearization strategy	Sensitive element	Sensitivity (V/T)	$\sqrt{AS_T^{1\text{Hz}}}$ ( $\mu\text{m nT}/\sqrt{\text{Hz}}$ )
Our work	Compensated magnetic anisotropy	TMR	12	4298
[28]	Shape anisotropy	TMR	4.5	6753
[5]	Superparamagnetism	TMR	10 <sup>a</sup>	3008
[24]	Magnetic vortex state	TMR	3	3125
[29]	Soft pinned free layer	TMR	30 <sup>a</sup>	7019
[30]	Shape anisotropy	TMR	1.5 <sup>a</sup>	4048
[11]	Compensated magnetic anisotropy	AHE	2.5	1520 <sup>b</sup>
[12]	Compensated magnetic anisotropy	AHE	1.6	2520

<sup>a</sup>Sensitivity measured from dc transfer curve.

<sup>b</sup>Under bias magnetic field of 12 Oe.

turns out to be a good candidate combining high sensitivity and good field detectability. Nevertheless, the scaling relation between low-frequency noise and sensitivity, as shown in Fig. 4(f), is quadratic. For sensors with quadratic scaling relation, higher sensitivity does not provide better low-frequency detectability [5,11,24].

We further measure the sensitivities of four MTJs with multiple  $t_{\text{CFB}}$  and  $T_a$  values, with  $t_W = 6 \text{ \AA}$  fixed. For a fair comparison, the maximum sensitivity  $S_P$  in a  $\pm 50$  Oe field range at each measurement temperature is recorded, since the offset field changes under different  $T_a$  in Fig. 1(c). As shown in Fig. 5(a),  $S_P$  for all samples first increases then decreases with measurement temperature, yet the peak positions are different. Further, we determine the in-plane saturation field  $H_S$  from the area between the hysteresis loop and the magnetic field axis [22,24] as an effective indicator of the PMA strength. In Fig. 5(b), while  $H_S$  varies for various samples under different measurement temperatures, the peak of  $S_P$  always falls in the same region of

$H_S$ . With such a clear correlation between  $S_P$  and  $H_S$ , the desired sensitivity and operating temperature of a MTJ sensor can be reached by tuning  $H_S$ , through the layer thickness and annealing conditions.

On the other hand, in this MTJ with interfacial PMA, random telegraph noise (RTN) exists with a Lorentzian spectrum, under a saturation field of 400 Oe where magnetic noise is suppressed. Experimentally, we measure a single MTJ with the same layer structure as the one in Fig. 4, in a circular shape of 5  $\mu\text{m}$  in diameter. The temperature-dependent noise spectrum is shown in Fig. 6(a). At 150 K, the noise conforms to a typical  $1/f$  relation. At 300 K, a bump appears due to the RTN, with a roll-off frequency near 10 Hz. As the temperature rises to 380 K, the roll-off frequency gradually shifts to higher frequencies of a few hundred hertz, and the bump amplitude drops. Corresponding time-domain signals are shown in the inset. At 300 K, two-level flipping is evident, with a long relaxation time near 0.1 s in one state; at 380 K,

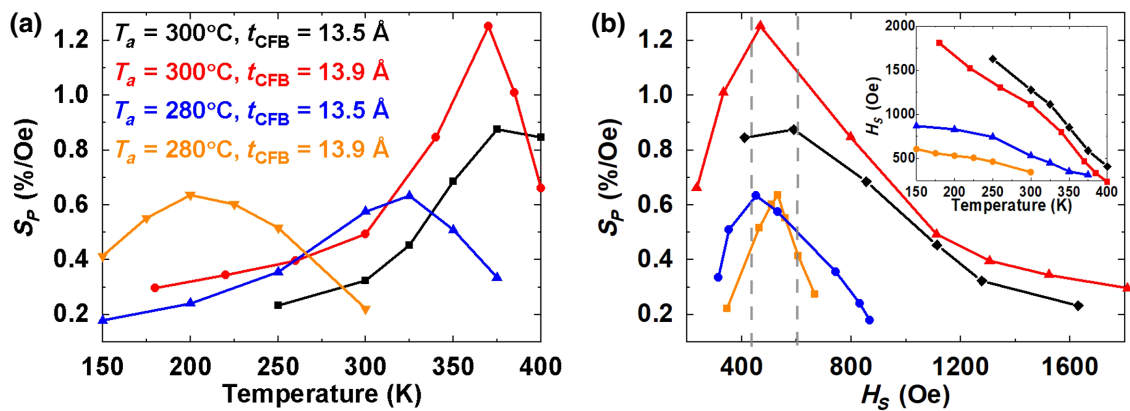


FIG. 5. (a) Peak sensitivity  $S_P$  at different temperatures for MTJs with various top Co-Fe-B layer thickness  $t_{\text{CFB}}$  and annealing temperature  $T_a$ . (b) Relationship between  $S_P$  and the in-plane magnetic saturation field  $H_S$  for the MTJs in (a). The inset shows  $H_S$  versus temperature.

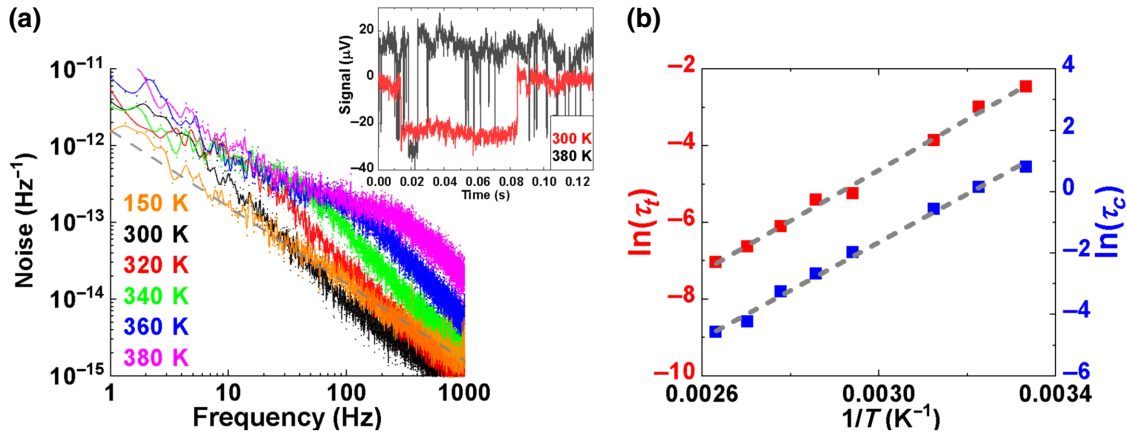


FIG. 6. (a) The Lorentzian spectrum of RTN in a single MTJ at saturation fields, with its corresponding time-domain signal shown in the inset. (b) The relaxation time in two states  $\ln(\tau_t)$ ,  $\ln(\tau_c)$  as a function of the inverse of temperature.

the flipping becomes more rapid with a 1-ms relaxation time.

RTN in MTJs is usually contributed by magnetic quasistable domain states in the free layer [31], but here we attribute RTN to an electrical generation-recombination (GR) process, as the MTJ is magnetically saturated. First, the energy of electrons in the conductive state of the MTJ can be altered by  $eV$  due to the bias voltage  $V$  [32,33]. During the tunneling process across the barrier, the conducting

electrons may be trapped by localized states either inside the MgO barrier [34,35] or at the Co-Fe-B/MgO interface [35], with a corresponding energy barrier preventing the flipping between the trapped state and the conductive state. Electrons get trapped by chance and return to the conductive state after a relaxation time. Such a GR process leads to a fluctuation in the charge carrier density and corresponding two-level voltage signals, which can be described as [36]

$$\begin{cases} \tau_t = \tau_0 \exp\left(\frac{\Delta E_1}{\gamma k_B T}\right) \\ \tau_c = \tau_0 \exp\left(\frac{\Delta E_2 + eV}{\gamma k_B T}\right) \\ V = a + bT \end{cases} \Rightarrow \begin{cases} \ln(\tau_t) = \frac{\Delta E_1}{\gamma k_B} \left(\frac{1}{T}\right) + \ln(\tau_0) \\ \ln(\tau_c) = \frac{\Delta E_2 + ea}{\gamma k_B} \left(\frac{1}{T}\right) + \frac{b}{\gamma k_B} + \ln(\tau_0), \end{cases} \quad (1)$$

where  $\tau_t$ ,  $\tau_c$  are the relaxation times of the trapping state and conductive state, respectively, where electrons spend much less time being locally trapped.  $T$  is the temperature,  $\tau_0$  an attempt time in the nanosecond range for an electron migration process, and  $\gamma$  an empirical constant. In our experimental setup, the bias voltage changes when the tunneling resistance of the MTJ decreases with rising temperature [2], with a temperature coefficient much larger than the serial resistor. The relation between bias voltage and temperature is thus calibrated to be  $V = a + bT$ , where  $a = 0.3$  V and  $b = -1.87 \times 10^{-4}$  V/K. Such small voltage change should have a negligible effect on the overall sensing properties [37].  $\Delta E_1$  is the energy barrier that a trapped electron needs to overcome before flipping into the conductive state, and such barrier is  $\Delta E_2 + eV$  for electrons in the conductive state to flip back into the

trapped state. To verify this model, we collect the average relaxation time  $\tau_t$ ,  $\tau_c$  in 30 s at various temperatures. The results are plotted in Fig. 6(b) on a semilog scale where an expected linear relation is found between  $\ln(\tau_t)$ ,  $\ln(\tau_c)$  and  $1/T$ . If we further assume that  $\Delta E_2 \approx \Delta E_1$ , the fitting indicates  $\Delta E_1 = \Delta E_2 = 2.59 \times 10^{-19}$  J and  $\gamma = 2.84$ . In addition, multiple Lorentzian spectra in Fig. 6(a) can be reconstructed by general RTN theory:

$$S(f) = \frac{4(\Delta V)^2}{(\tau_t + \tau_c)[(1/\tau_t + 1/\tau_c)^2 + (2\pi f)^2]}, \quad (2)$$

where  $\Delta V$  is the voltage difference between two flipping states in the inset of Fig. 6(a).

#### IV. CONCLUSION

We reveal the PMA strength in a MTJ free layer versus its spacer layer thickness, free layer thickness, and annealing temperature, which provide levers to manipulate the magnetic anisotropy in the free layer. The inhomogeneity of PMA, the competition between PMA and shape anisotropy, and its correlation with sensing performances are discussed in detail. In multiple MTJ sensors with different fabrication conditions, we illustrate that the compensation of magnetic anisotropy can be used as a means to increase the field detectability to  $1.8 \text{ nT}/\sqrt{\text{Hz}}$  at 100 kHz, and to modify the operating temperature of a MTJ device. Moreover, RTN is observed and explained by an electrical generation-recombination process in this device. Such a voltage-dependent RTN could potentially be utilized in true random number generators, similarly to the utilization of thermal noise in superparamagnetic MTJs [38].

#### ACKNOWLEDGMENTS

The work is supported by the National Science Foundation (NSF) under Grant No. OMA-1936221. Y.Z. acknowledges support from Fermilab-Graduate Instrumentation Research Award under DOE Grant No. DEAC05-00OR22725. We used the Heidelberg MLA150 Maskless Aligner supported by the National Science Foundation (Grant No. DMR-1827453).

- [1] B. Dieny, I. L. Prejbeanu, K. Garello, P. Gambardella, P. Freitas, R. Lehnendorff, W. Raberg, U. Ebels, S. O. Demokritov, and J. Akerman, Opportunities and challenges for spintronics in the microelectronics industry, *Nat. Electron.* **3**, 446 (2020).
- [2] G. Xiao, in *Spintronics Handbook: Spin Transport and Magnetism*, 2nd Ed. (2019), p. 385
- [3] X. Liu, C. Ren, and G. Xiao, Magnetic tunnel junction field sensors with hard-axis bias field, *J. Appl. Phys.* **92**, 4722 (2002).
- [4] Y. Lu, R. Altman, A. Marley, S. Rishton, P. Trouilloud, G. Xiao, W. Gallagher, and S. Parkin, Shape-anisotropy-controlled magnetoresistive response in magnetic tunnel junctions, *Appl. Phys. Lett.* **70**, 2610 (1997).
- [5] Y. Zhang, G. He, X. Zhang, and G. Xiao, Magnetotransport and electronic noise in superparamagnetic magnetic tunnel junctions, *Appl. Phys. Lett.* **115**, 022402 (2019).
- [6] Z. Zeng, P. Khalili Amiri, J. Katine, J. Langer, K. Wang, and H. Jiang, Nanoscale magnetic tunnel junction sensors with perpendicular anisotropy sensing layer, *Appl. Phys. Lett.* **101**, 062412 (2012).
- [7] W. Zhang, G. Xiao, and M. J. Carter, Two-dimensional field-sensing map and magnetic anisotropy dispersion in magnetic tunnel junction arrays, *Phys. Rev. B* **83**, 144416 (2011).
- [8] D. Mazumdar, W. Shen, X. Liu, B. Schrag, M. Carter, and G. Xiao, Field sensing characteristics of magnetic tunnel junctions with (001) MgO tunnel barrier, *J. Appl. Phys.* **103**, 113911 (2008).
- [9] D.-T. Quach, Q.-H. Tran, K. Møhave, and D.-H. Kim, Perpendicular magnetic anisotropy and the magnetization process in CoFeB/Pd multilayer films, *J. Phys. D: Appl. Phys.* **47**, 445001 (2014).
- [10] O. Bultynck, M. Manfrini, A. Vaysset, J. Swerts, C. J. Wilson, B. Sorée, M. Heyns, D. Mocuta, I. P. Radu, and T. Devolder, Instant-On Spin Torque in Noncollinear Magnetic Tunnel Junctions, *Phys. Rev. Appl.* **10**, 054028 (2018).
- [11] Y. Zhang, K. Wang, and G. Xiao, Noise characterization of ultrasensitive anomalous Hall effect sensors based on  $\text{Co}_{40}\text{Fe}_{40}\text{B}_{20}$  thin films with compensated in-plane and perpendicular magnetic anisotropies, *Appl. Phys. Lett.* **116**, 212404 (2020).
- [12] K. Wang, Y. Zhang, and G. Xiao, Anomalous Hall Sensors with High Sensitivity and Stability Based on Interlayer Exchange-Coupled Magnetic Thin Films, *Phys. Rev. Appl.* **13**, 064009 (2020).
- [13] M. Wang, Y. Zhang, X. Zhao, and W. Zhao, Tunnel junction with perpendicular magnetic anisotropy: Status and challenges, *Micromachines* **6**, 1023 (2015).
- [14] W. Skowroński, M. Czapkiewicz, S. Ziętek, J. Chęciński, M. Frankowski, P. Rzeszut, and J. Wrona, Understanding stability diagram of perpendicular magnetic tunnel junctions, *Sci. Rep.* **7**, 1 (2017).
- [15] M. Wang, W. Cai, K. Cao, J. Zhou, J. Wrona, S. Peng, H. Yang, J. Wei, W. Kang, and Y. Zhang, Current-induced magnetization switching in atom-thick tungsten engineered perpendicular magnetic tunnel junctions with large tunnel magnetoresistance, *Nat. Commun.* **9**, 1 (2018).
- [16] T. Nakano, M. Oogane, H. Naganuma, and Y. Ando, Systematic investigation on correlation between sensitivity and nonlinearity in magnetic tunnel junction for magnetic sensor, *IEEE Trans. Magn.* **51**, 1 (2015).
- [17] P. Wisniewski, J. Wrona, T. Stobiecki, S. Cardoso, and P. Freitas, Magnetic tunnel junctions based on out-of-plane anisotropy free and in-plane pinned layer structures for magnetic field sensors, *IEEE Trans. Magn.* **48**, 3840 (2012).
- [18] G. He, Y. Zhang, L. Qian, G. Xiao, Q. Zhang, J. C. Santamarina, T. W. Patzek, and X. Zhang, Picotesla magnetic tunneling junction sensors integrated with double staged magnetic flux concentrators, *Appl. Phys. Lett.* **113**, 242401 (2018).
- [19] J. Chatterjee, S. Auffret, R. Sousa, P. Coelho, I.-L. Prejbeanu, and B. Dieny, Novel multifunctional RKKY coupling layer for ultrathin perpendicular synthetic antiferromagnet, *Sci. Rep.* **8**, 1 (2018).
- [20] J. Chen, S. Peng, D. Xiong, H. Cheng, H. Zhou, Y. Jiang, J. Lu, W. Li, and W. Zhao, Correlation of interfacial perpendicular magnetic anisotropy and interlayer exchange coupling in CoFe/W/CoFe structures, *J. Phys. D: Appl. Phys.* **53**, 334001 (2020).
- [21] S. S. Parkin, Systematic Variation of the Strength and Oscillation Period of Indirect Magnetic Exchange Coupling through the 3d, 4d, and 5d Transition Metals, *Phys. Rev. Lett.* **67**, 3598 (1991).
- [22] J. G. Alzate, P. Khalili Amiri, G. Yu, P. Upadhyaya, J. A. Katine, J. Langer, B. Ocker, I. N. Krivorotov, and K. L. Wang, Temperature dependence of the voltage-controlled



- perpendicular anisotropy in nanoscale MgO|CoFeB|Ta magnetic tunnel junctions, *Appl. Phys. Lett.* **104**, 112410 (2014).
- [23] K.-M. Lee, J. W. Choi, J. Sok, and B.-C. Min, Temperature dependence of the interfacial magnetic anisotropy in W/CoFeB/MgO, *AIP Adv.* **7**, 065107 (2017).
- [24] G. He, Y. Zhang, and G. Xiao, Nonhysteretic Vortex Magnetic Tunnel Junction Sensor with High Dynamic Reserve, *Phys. Rev. Appl.* **14**, 034051 (2020).
- [25] H. Sepehri-Amin, T. Ohkubo, M. Gruber, T. Schrefl, and K. Hono, Micromagnetic simulations on the grain size dependence of coercivity in anisotropic Nd-Fe-B sintered magnets, *Scr. Mater.* **89**, 29 (2014).
- [26] H. Liu, R. Wang, P. Guo, Z. Wen, J. Feng, H. Wei, X. Han, Y. Ji, and S. Zhang, Manipulation of magnetization switching and tunnel magnetoresistance via temperature and voltage control, *Sci. Rep.* **5**, 18269 (2015).
- [27] Z. Lei, G. Li, W. F. Egelhoff, P. Lai, and P. W. Pong, Review of noise sources in magnetic tunnel junction sensors, *IEEE Trans. Magn.* **47**, 602 (2011).
- [28] W. Z. Zhang, Q. Hao, and G. Xiao, Low-frequency noise in serial arrays of MgO-based magnetic tunnel junctions, *Phys. Rev. B* **84**, 094446 (2011).
- [29] J. P. Valadeiro, J. Amaral, D. C. Leitao, R. Ferreira, S. F. Cardoso, and P. J. P. Freitas, Strategies for ptesla field detection using magnetoresistive sensors with a soft pinned sensing layer, *IEEE Trans. Magn.* **51**, 1 (2015).
- [30] S.-H. Liou, D. Sellmyer, S. E. Russek, R. Heindl, F. Da Silva, J. Moreland, D. P. Pappas, L. Yuan, and J. Shen, in *SENSORS, 2009 IEEE* (IEEE, 2009), pp. 1848–1851.
- [31] T. Arakawa, T. Tanaka, K. Chida, S. Matsuo, Y. Nishihara, D. Chiba, K. Kobayashi, T. Ono, A. Fukushima, and S. Yuasa, Low-frequency and shot noises in CoFeB/MgO/CoFeB magnetic tunneling junctions, *Phys. Rev. B* **86**, 224423 (2012).
- [32] Y. Sakuraba, K. Takanashi, Y. Kota, T. Kubota, M. Oogane, A. Sakuma, and Y. Ando, Evidence of Fermi level control in a half-metallic Heusler compound  $\text{Co}_2\text{MnSi}$  by Al-doping: Comparison of measurements with first-principles calculations, *Phys. Rev. B* **81**, 144422 (2010).
- [33] Y. Lu, X. Li, G. Xiao, R. Altman, W. Gallagher, A. Marley, K. Roche, and S. Parkin, Bias voltage and temperature dependence of magnetotunneling effect, *J. Appl. Phys.* **83**, 6515 (1998).
- [34] J. Teixeira, J. Ventura, J. Araujo, J. Sousa, P. Wisniowski, S. Cardoso, and P. Freitas, Resonant Tunneling through Electronic Trapping States in Thin MgO Magnetic Junctions, *Phys. Rev. Lett.* **106**, 196601 (2011).
- [35] Z. Diao, J. F. Feng, H. Kurt, G. Feng, and J. M. D. Coey, Reduced low frequency noise in electron beam evaporated MgO magnetic tunnel junctions, *Appl. Phys. Lett.* **96**, 202506 (2010).
- [36] C. Rogers and R. Buhrman, Composition of 1 f Noise in Metal-Insulator-Metal Tunnel Junctions, *Phys. Rev. Lett.* **53**, 1272 (1984).
- [37] W. Skowroński, P. Wiśniowski, T. Stobiecki, S. Cardoso, P. P. Freitas, and S. van Dijken, Magnetic field sensor with voltage-tunable sensing properties, *Appl. Phys. Lett.* **101**, 192401 (2012).
- [38] D. Vodenicarevic, N. Locatelli, A. Mizrahi, J. S. Friedman, A. F. Vincent, M. Romera, A. Fukushima, K. Yakushiji, H. Kubota, and S. Yuasa, Low-Energy Truly Random Number Generation with Superparamagnetic Tunnel Junctions for Unconventional Computing, *Phys. Rev. Appl.* **8**, 054045 (2017).